

# Towards RAW Object Detection in Diverse Conditions

Zhong-Yu Li<sup>1</sup> Xin Jin<sup>1</sup> Boyuan Sun<sup>1</sup> Chun-Le Guo<sup>1</sup> Ming-Ming Cheng<sup>1</sup>  
<sup>1</sup>VCIP, School of Computer Science, Nankai University  
<https://github.com/lzyhha/AODRaw>

## Abstract

Existing object detection methods often consider sRGB input, which was compressed from RAW data using ISP originally designed for visualization. However, such compression might lose crucial information for detection, especially under complex light and weather conditions. We introduce the AODRaw dataset, which offers 7,785 high-resolution real RAW images with 135,601 annotated instances spanning 62 categories, capturing a broad range of indoor and outdoor scenes under 9 distinct light and weather conditions. Based on AODRaw that supports RAW and sRGB object detection, we provide a comprehensive benchmark for evaluating current detection methods. We find that sRGB pre-training constrains the potential of RAW object detection due to the domain gap between sRGB and RAW, prompting us to directly pre-train on the RAW domain. However, it is harder for RAW pre-training to learn rich representations than sRGB pre-training due to the camera noise. To assist RAW pre-training, we distill the knowledge from an off-the-shelf model pre-trained on the sRGB domain. As a result, we achieve substantial improvements under diverse and adverse conditions without relying on extra pre-processing modules.

## 1. Introduction

Real-world object detection is a fundamental task in computation vision. Significant advancements have been made in this field with public datasets like COCO [21] and VOC [10]. However, these datasets have predominantly focused on sRGB images, which lose some critical information compared to RAW images. The sensor first captures original RAW images with a high bit depth in a typical camera. An image signal processor (ISP) then compresses these RAW images into 8-bit sRGB images. Unlike compressed sRGB images, RAW images retain a higher bit depth and thus preserve more distinguishable information, which is crucial for computer vision tasks, particularly in challenging light and weather conditions. Moreover, inference on RAW images can reduce the time and power required by

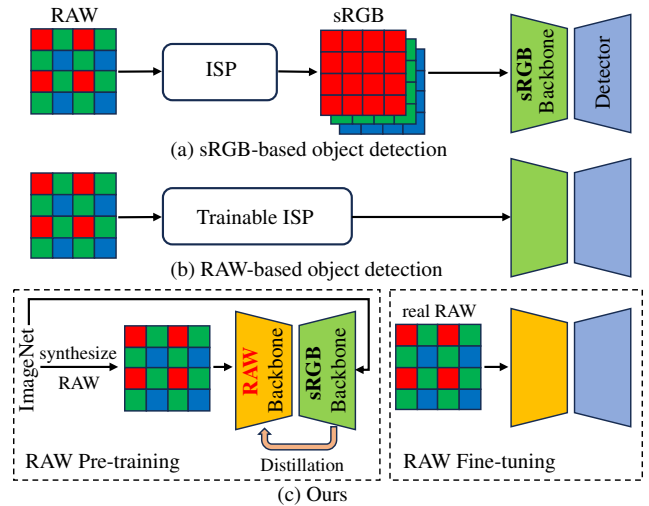


Figure 1. (a) Traditional sRGB-based object detection relies on 8-bit sRGB images, which are compressed from RAW images and lose detailed information. (b) Previous RAW-based methods utilize a trainable image signal processor (ISP) to adapt models pre-trained on the sRGB domain to the RAW domain. (c) We pre-train models on the RAW domain, achieving excellent performance on RAW object detection without requiring ISP modules.

ISP. Thus, RAW-based object detection has gained attention, especially in adverse conditions. However, exploration in this field remains limited.

The scarcity of relevant datasets is the key factor limiting the development of RAW-based object detection. However, collecting RAW images for object detection requires much more costs than sRGB images. For example, RAW images cannot be collected from picture websites like the sRGB-based dataset COCO [21]. Thus, taking pictures requires a lot of labor, especially in rare weather conditions. Due to the limitations of collecting and annotating images, many RAW object detection methods [8, 25] rely on synthesizing RAW images that lack the authentic noise patterns and dynamic range. The real RAW datasets [17, 26, 34] are also limited to the diversity. For example, LOD [17] and RAOD [34] datasets are annotated with only 8 and 6 categories, respectively. Moreover, some datasets focus on

outdoor scenes of daylight and low-light while neglecting other adverse conditions. Thus, existing methods have limited applications and cannot fully utilize the advantages of RAW images in handling adverse conditions.

To overcome these limitations, we propose a challenging dataset (**AODRaw**) for **A**dverse condition **O**bject **D**etection with **RAW** images. AODRaw collect real RAW images from various indoor and outdoor scenes, where 2 light conditions, including daylight and low-light, and 3 weather conditions, including clear, rain, and fog, are considered. Because multiple light and weather conditions may occur, 9 distinct conditions are collected. In total, we obtained 7,785 images and 135,601 annotated instances, with 6,504 images captured under adverse conditions. Meanwhile, our AODRaw is annotated with 62 categories, significantly exceeding existing datasets. The diversity of scenes and semantics can further facilitate the development of RAW-based object detection in the real world. Furthermore, we evaluate existing RAW object detection methods [8, 34] based on the AODRaw dataset.

With AODRaw, we aim to design a single model to detect objects across various conditions simultaneously, rather than training separate models for each condition in some previous approaches [8]. For RAW object detection, many methods usually transfer models pre-trained in the sRGB domain to the RAW domain using trainable adapters like neural ISP [8]. However, the domain gap between sRGB and RAW impedes models from understanding the intricate information in RAW images, while the added adapters also introduce extra costs. Some methods [34] train models from scratch, yet limited data availability constrains performance and generalization.

Differently, we explore pre-training on the RAW domain to reduce the domain gap between pre-training and fine-tuning, achieving notable improvements without any adapters. However, it is more difficult for models to learn high-quality representations from RAW images than sRGB images due to the camera noise. To this end, we propose to distill representations from an off-the-shelf model pre-trained on the sRGB domain to mitigate this difficulty. Taking ConvNext-T [24] and Cascade RCNN [3], sRGB-based object detection achieves 34.0% AP on AODRaw. RAW object detection improves the performance to 34.8% AP through our RAW pre-training. To summarize, our main contributions are as follows:

- We propose AODRaw, a high-quality dataset for RAW object detection under various light and weather conditions. The dataset comprises diverse and complex images collected from various indoor and outdoor scenes.
- The AODRaw supports research across multiple tasks, including RAW object detection and sRGB object detection under adverse conditions. We evaluate the performance of existing object detection methods on these tasks.

- We pre-train models on RAW images via cross-domain distillation, achieving significant improvements without needing adapters such as neural ISPs.

## 2. Related Works

### 2.1. Object Detection

Mainstream object detection methods can be divided into two categories, *i.e.*, multi-stage and one-stage detectors. The multi-stage detectors, *e.g.*, R-CNN series [3, 28, 30], first generate region proposals and then refine them in subsequent stages. Cascade R-CNN [3] further extends this process via multiple refinement stages, progressively improving localization and classification accuracy. Although these methods achieve high accuracy, they have the drawback of slow inference. One-stage methods, such as YOLO [11] and RetinaNet [22], directly predict object locations and categories, enabling faster inference but at a trade-off in precision. In addition, transformer-based approaches like Deformable DETR [38] have emerged and leverage self-attention mechanisms to model spatial relationships in the image while requiring longer training times. Because these methods are primarily designed for sRGB images, we further evaluates these classic methods in the RAW domain.

### 2.2. RAW Object Detection

RAW object detection, which leverages unprocessed sensor data, has gained attention due to its potential in challenging light and weather conditions. However, the field lacks large-scale datasets for pre-training models on RAW images, which is essential for modern object detection methods. Thus, some methods [34] train detectors from scratch using real-time detectors [11]. Due to camera noise and the limited quantity of RAW images, these methods may converge slowly and face limitations in performance. The other methods [33, 35, 36] adapt models pre-trained on sRGB images to the RAW domain. Among them, some propose a differentiable image signal processor (ISP) [8, 9, 13, 25, 27, 31] for pre-processing RAW images. Fine-tuning models by synthesizing RAW images from COCO [5, 20] also helps mitigate the domain gap. However, the sRGB pre-training still limits the ability to understand RAW images that contain much more information than sRGB images, and the ISP modules add extra computation costs. Thus, we explore pre-training models on RAW images.

### 2.3. RAW Object Detection Datasets

Existing datasets for object detection, like COCO [21], primarily collect sRGB images. Although these datasets have driven significant progress in object detection, sRGB images lack the detailed information available in RAW images, which can be particularly beneficial in adverse conditions. Due to the scarcity of RAW datasets, many meth-

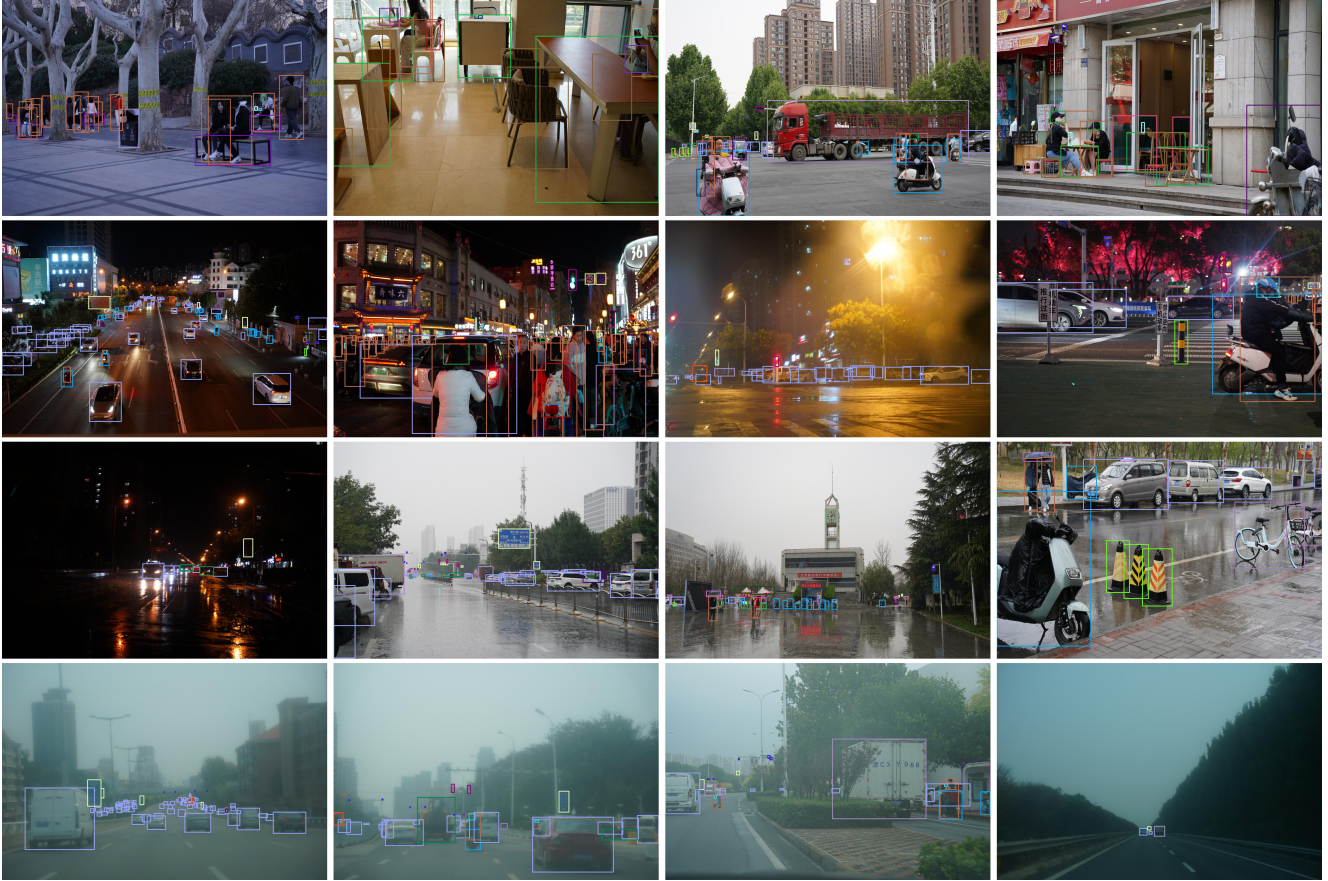


Figure 2. Example of the images in the AODRaw. From top to bottom, we show daylight, low-light, rain, and fog conditions, respectively. A part of the images are taken under multiple conditions. For example, the first one in the third row is taken in low-light and rain conditions. More examples for each condition can be found in the supplementary material.

ods [8, 25] rely on synthetic datasets for RAW detection research. Then, a few RAW datasets have been proposed. For example, [37] collects images in low-light conditions, and [1] collects driving images of high dynamic range in fog conditions. The PASCALRAW [26] dataset is collected similarly to the PASCAL VOC [10], providing 4,259 images in daylight. The LOD [17] captures 2,230 paired images in daylight and low-light conditions. RAOD [34] has 25,207 annotated driving images but only covers 6 categories and 2 light conditions. Specific conditions, driving-focused scenes, or a narrow range of annotated categories limit these datasets.

### 3. AODRaw Dataset

#### 3.1. Data Collection

**Diverse conditions.** We construct a challenging dataset for RAW-based object detection under adverse and diverse conditions. Specifically, we consider 2 light conditions, *i.e.*, daylight and low-light, and 3 weather conditions, *i.e.*, clear,

rain, and fog. For different light conditions, we capture both indoor and outdoor images. Because multiple conditions may co-occur, we finally collect 7,785 real RAW images and the corresponding sRGB images across 9 combined conditions, as shown in Tab. 2. For example, the image in the third row and first column of Fig. 2 is in rain and low-light conditions.

**Data diversity.** In addition to condition diversity, we capture images across various cities and scenes to ensure broad data diversity. As shown in Fig. 2, some images are taken in traffic scenes, while others cover gardens, universities, libraries, streets, and other indoor scenes.

**Data annotation.** We follow the annotation format of the COCO dataset [21] to annotate bounding boxes in images across 62 categories commonly seen in daily life.

#### 3.2. Data Analysis

In this section, we analyze the AODRaw dataset and compare it with two previous object detection datasets, *i.e.*, COCO [21] of sRGB object detection and RAOD [34] of



Dataset	Resolution	Images	Categories	Instances	Instances per image	Conditions
OnePlus [36]	4640 × 3480	141	5	1,228	8.7	1 (low-light)
PASCALRAW [26]	600 × 400	4,259	3	6,550	1.5	1 (daylight)
LOD [17]	1200 × 800	2,230	8	9,726	4.4	2 (daylight and low-light)
RAOD [34]	2880 × 1856	25,207	6	237,379	9.4	2 (daylight and low-light)
AODRaw (Ours)	6000 × 4000	7,785	62	135,601	17.4	9 (in Tab. 2)

Table 1. Comparison with existing RAW datasets.

Brightness	Indoor		Outdoor						Total	
	daylight	low-light	daylight			low-light				
Weather	-	-	clear	fog	rain	fog+rain	clear	fog	rain	
Images	477	1,210	804	1,110	1,252	244	1,842	325	521	7,785
Instances	4,992	10,195	18,575	23,636	24,107	5,381	37,282	4,513	6,920	135,601

Table 2. The number of images per condition.

RAW object detection. In the supplementary material, we show the detailed analysis about each condition.

**Diverse scenes.** As summarized in Tab. 2, AODRaw covers 9 conditions, including 2 light conditions, 3 weather conditions, and different combinations. Compared to existing datasets for RAW object detection, which mainly focus on outdoor scenes in daylight or low-light, as shown in Tab. 1, AODRaw has a greater diversity, presenting a more challenging task. Moreover, the scenes in AODRaw are varied and complex. As shown in Fig. 3a and Fig. 3b, images in AODRaw contain varying categories and instances, with up to 19 categories and 327 instances in an image. On average, there are 17.4 instances per image as shown in Tab. 1, exceeding existing datasets.

**Increased category diversity.** AODRaw includes 62 categories, a significantly higher number than most existing RAW object detection datasets, as shown in Tab. 1. Meanwhile, as shown in Fig. 3d, the distribution of categories exhibits a long-tail pattern, further increasing the challenge of RAW object detection in this dataset.

**Object scales.** The instances in the AODRaw vary widely in size, as shown in Fig. 3c, with a notably larger proportion of small objects than in previous datasets. This variance requires the detectors to extract multi-scale representations, increasing the complexity of the detection task.

**Spatial distribution.** The instances in the AODRaw dataset are more uniformly distributed in the images, as shown in Fig. 4. This uniform spatial distribution helps reduce spatial bias. Additionally, there is a slight bias towards the bottom of images, as most images are captured in outdoor scenes.

**Light distribution.** The distribution of lightness, calculated as the average gray value of sRGB images, is shown in Fig. 3e and Fig. 3f. The distribution reveals a broad range

of light conditions in AODRaw.

### 3.3. Data Split

The dataset is split for training and testing sets with a 7:3 ratio. To ensure that each split contains sufficient images of each condition, we split each condition individually and then merge the splitting results. As a result, we obtained 5,445 training images and 2,340 testing images, which contain 94,949 and 40,652 instances, respectively.

## 4. Benchmark

### 4.1. Implementation Details

**Model training.** We implement all object detection methods using a popular code base, mmdetection [4]. The models are trained for 48 epochs with a batch size of 16, except for Deformable DETR [38], which is trained for 100 epochs. Please refer to the supplementary material for more hyper-parameters. In addition, the RAW images are originally saved in the bayer pattern with the shape of  $1 \times H \times W$ , where  $H$  and  $W$  mean the height and width of images. To be compatible with existing models, we transform the RAW images into  $3 \times H \times W$  using demosaicing following [34]. Following [20], the RAW images are further processed through gamma correction for faster convergence.

**Image resolution.** The images in the AODRaw dataset are recorded at a resolution of  $6000 \times 4000$ . It is unrealistic to feed such huge images into the detectors. Thus, we adopt two experiment settings: 1) down-sampling the images into a lower resolution of  $2000 \times 1333$  following the approach in [34], and 2) slicing the images into a collection of  $1280 \times 1280$  patches with a patch overlap of 300 and ignoring the objects whose IoU with the sliced images is lower than 0.4,



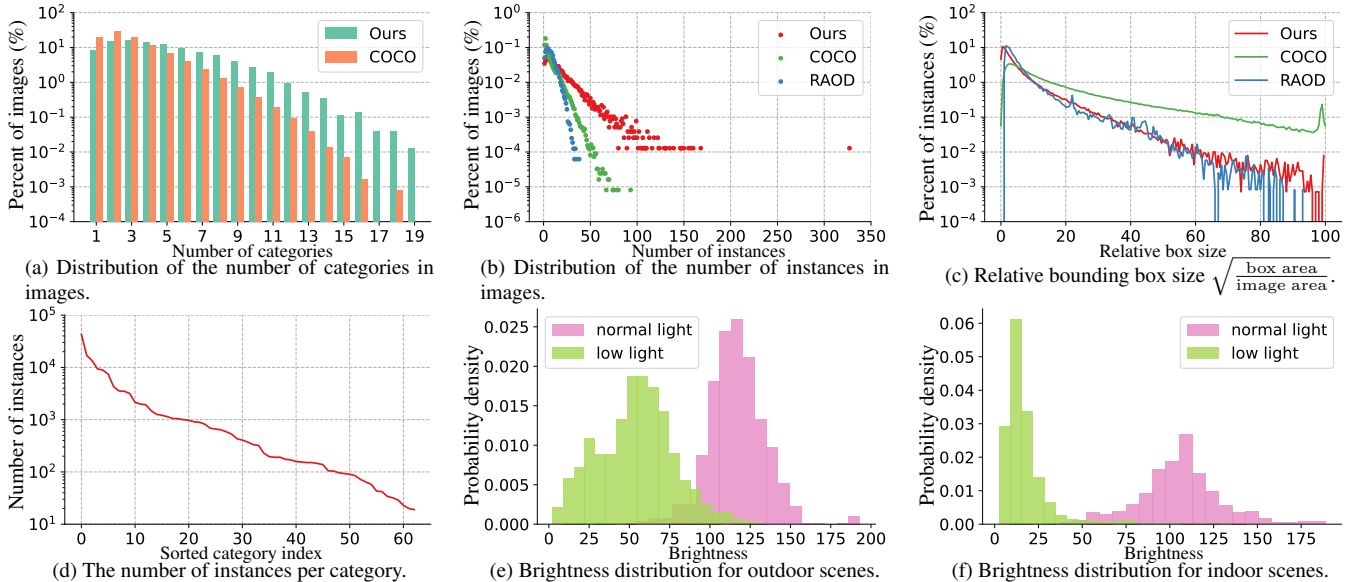


Figure 3. Statistics indicate that our AODRaw dataset contains increased category and instance diversity.

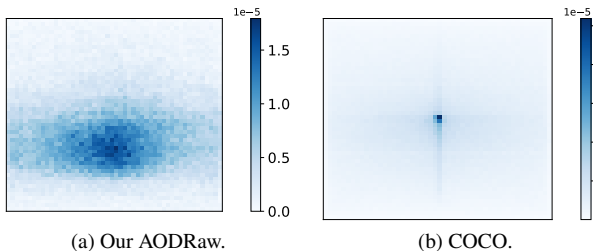


Figure 4. The distribution of object centers.

resulting in 71,782 images and 417,781 instances. The first setting supports faster training, but too tiny objects with an area of less than  $32^2$  are ignored because they will disappear after down-sampling. The second requires more time for training, but it can fully use high-quality annotations and support tiny object detection [7]. In the following, we adopt down-sampling by default.

**Evaluation protocol.** We evaluate the models using the popular metric Average Precision (AP) [4, 21], along with  $AP_{75}$  and  $AP_{50}$  at the IoU threshold of 0.75 and 0.50. About  $AP_s$ ,  $AP_m$ , and  $AP_l$  for small, medium, and large objects, we set object area ranges as  $[0, 128^2)$ ,  $[128^2, 320^2)$ , and  $[320^2, +\infty)$ , respectively, when using the setting of down-sampling images. When slicing images, the ranges are set as  $[0, 64^2)$ ,  $[64^2, 160^2)$ , and  $[160^2, +\infty)$ , respectively. To facilitate object detection in adverse conditions, we also report  $AP_{low}$ ,  $AP_{rain}$ , and  $AP_{fog}$  for low-light, rain, and fog conditions, apart from  $AP_{normal}$  for the normal condition (the combination of daylight and clear weather).

## 4.2. Analysis

With AODRaw, we analyze the performances of various detectors for object detection with both sRGB and RAW images, as shown in Tab. 3. We evaluate some popular and milestone works, including multi-stage detectors (Faster RCNN [28], Sparse RCNN [30], and Cascade RCNN [3]), one-stage detectors (RetinaNet [22] and GFocal [19]), and transformer-based detectors (Deformable DETR [38]).

**sRGB object detection in adverse conditions.** Cascade RCNN achieves superior performance among the evaluated methods, with 25.6% AP and 27.3%  $AP_{normal}$ . However, the  $AP_{low}$ ,  $AP_{rain}$ , and  $AP_{fog}$  are only 23.8%, 24.7%, and 20.4%, showing that the adverse conditions bring more challenges. More advanced backbones like ConvNeXt and Swin-T can improve performance. For example, ConvNeXt-T outperforms ResNet by 9.7% in  $AP_{normal}$ , but with lower improvements on adverse conditions, *i.e.*, 7.7%  $AP_{low}$ , 6.2%  $AP_{rain}$ , and 6.8%  $AP_{fog}$ . Such a gap shows the drawback of sRGB images in adverse conditions.

**RAW object detection in adverse conditions.** It is inappropriate to adopt models pre-trained on sRGB images when fine-tuning on RAW images. For example, RAW-based Cascade RCNN only achieves 33.7% AP when using sRGB pre-training, which is lower than 34.0% of the sRGB-based method. This phenomenon is partially caused by the domain gap between sRGB and RAW. As shown in Tab. 4, the detector trained on one domain will be significantly degraded when testing on another, showing that the RAW and sRGB domain models cannot generalize well to each other.

To overcome the domain gap, previous object detection methods in the RAW domain usually connect a neural image signal processor (ISP) with detectors, where the ISP

Method	Backbone	Pre-Train	Fine-Tune	AP	AP <sub>50</sub>	AP <sub>75</sub>	AP <sub>s</sub>	AP <sub>m</sub>	AP <sub>l</sub>	AP <sub>normal</sub>	AP <sub>low</sub>	AP <sub>rain</sub>	AP <sub>fog</sub>
Faster RCNN [28]	ResNet-50 [14]			23.3	41.3	23.7	13.1	30.8	36.4	26.0	22.0	24.4	19.6
Retinanet [22]	ResNet-50 [14]			19.1	33.6	19.2	10.1	26.6	29.5	21.5	17.8	19.2	16.5
GFocal [19]	ResNet-50 [14]	sRGB	sRGB	24.2	40.3	24.7	13.3	31.9	37.0	26.5	22.3	24.1	21.1
Sparse RCNN [30]	ResNet-50 [14]			15.6	28.3	15.0	7.2	22.1	28.9	17.9	15.0	14.6	12.6
Deformable DETR [38]	ResNet-50 [14]			16.6	31.9	15.6	7.7	23.9	30.1	18.3	15.2	16.4	13.1
Cascade RCNN [3]	ResNet-50 [14]			25.6	41.4	26.4	13.7	32.4	38.3	27.3	23.8	24.7	20.4
Faster RCNN [28]	Swin-T [23]			28.4	50.1	28.8	15.6	35.9	42.6	32.0	26.0	27.2	23.3
Faster RCNN [28]	ConvNeXt-T [24]			29.7	51.7	30.1	17.1	37.3	45.4	33.1	28.3	27.1	24.4
GFocal [19]	Swin-T [23]	sRGB	sRGB	30.1	48.9	30.6	16.3	38.0	44.4	32.7	28.1	28.2	24.5
GFocal [19]	ConvNeXt-T [24]			32.1	49.9	33.6	18.7	39.9	49.5	35.2	30.3	31.8	26.0
Cascade RCNN [3]	Swin-T [23]			32.0	50.2	34.0	17.5	40.1	46.3	35.4	30.0	28.2	25.0
Cascade RCNN [3]	ConvNeXt-T [24]			34.0	52.7	36.3	19.3	40.8	52.1	37.0	31.5	32.9	27.2
Faster RCNN [28]	Swin-T [23]			28.1	50.0	28.2	16.0	35.7	42.6	30.7	26.5	26.2	22.0
Faster RCNN [28]	ConvNeXt-T [24]			29.4	51.3	29.6	16.3	37.6	44.4	32.7	27.3	29.2	24.6
GFocal [19]	Swin-T [23]	sRGB	RAW	29.9	48.2	30.6	16.3	38.3	45.0	33.1	27.6	29.0	23.8
GFocal [19]	ConvNeXt-T [24]			31.5	50.0	32.9	17.9	39.5	48.4	34.9	29.4	32.2	26.7
Cascade RCNN [3]	Swin-T [23]			31.7	49.8	32.8	17.7	39.7	47.8	35.3	29.8	28.6	23.9
Cascade RCNN [3]	ConvNeXt-T [24]			33.7	52.0	35.9	18.6	41.7	51.3	36.8	31.3	31.3	27.2
Faster RCNN [28]	Swin-T [23]			28.6	50.2	28.5	15.6	36.9	43.1	32.1	26.7	27.6	23.2
Faster RCNN [28]	ConvNeXt-T [24]			30.2	52.3	31.0	17.0	39.1	46.9	33.8	27.7	30.2	26.6
GFocal [19]	Swin-T [23]	RAW	RAW	30.7	49.7	31.8	17.2	39.4	47.4	33.7	28.6	28.5	25.3
GFocal [19]	ConvNeXt-T [24]			32.1	50.4	33.4	17.7	40.6	49.6	35.8	29.9	32.8	27.1
Cascade RCNN [3]	Swin-T [23]			32.2	50.5	33.8	17.9	40.5	49.7	35.5	30.0	29.5	25.1
Cascade RCNN [3]	ConvNeXt-T [24]			34.8	53.3	36.7	20.6	42.8	52.5	37.7	32.1	36.1	28.4

Table 3. Evaluation of object detection using RGB images, with different pre-training and fine-tuning settings.

projects the images from RAW to the sRGB domain. In Tab. 5, we evaluate two recently proposed methods designed for RAW object detection, RAOD [34] and RAW-Adapter [8]. Results show that neural ISP can stimulate the potential of RAW images. For example, RAOD achieves 34.4% AP and outperforms the 34.0% AP of the sRGB-based method. In particular, RAOD achieves greater improvements in adverse conditions than the normal condition (0.9% AP<sub>low</sub>, 4.8% AP<sub>rain</sub>, and 2.2% AP<sub>fog</sub> vs 0.3% AP<sub>normal</sub>). However, the neural ISP incurs extra computational costs and cannot fill the gap between RAW and sRGB domains, preventing the knowledge learned by the pre-trained model from being fully utilized.

## 5. RAW Pre-training

### 5.1. Method

Based on the above analysis, we aim to overcome the gap between sRGB pre-training and RAW fine-tuning by directly pre-training the models on RAW images, enabling us to achieve superior performances without requiring pre-processing modules like neural ISP.

**Synthetic ImageNet-RAW.** Visual pre-training [14, 15] has

Training	Evaluation	AP	AP <sub>50</sub>	AP <sub>75</sub>
sRGB	sRGB	34.0	52.7	36.3
	RAW	28.0	43.2	29.6
RAW	sRGB	21.2	33.1	22.5
	RAW	34.8	53.3	36.7

Table 4. The domain gap between sRGB and RAW.

made huge progress with the help of large-scale datasets like ImageNet-1K [29] that has over one million images. However, it is unrealistic to collect real RAW datasets of comparable size to large-scale sRGB datasets. Thus, we synthesize a 16-bit RAW dataset from the ImageNet-1K for RAW pre-training, using the unprocessing method [2] that converts sRGB images to RAW images and simulates camera noise. We refer to the generated dataset as ImageNet-RAW. In the implementation, the unprocessed operation is inserted into the pipeline of data augmentations. Thus, we can randomly adjust the average brightness and simulated noise in each iteration so that models can generalize well across different conditions.

Method	Backbone	Neural ISP	AP	AP <sub>50</sub>	AP <sub>75</sub>	AP <sub>s</sub>	AP <sub>m</sub>	AP <sub>l</sub>	AP <sub>normal</sub>	AP <sub>low</sub>	AP <sub>rain</sub>	AP <sub>fog</sub>
Baseline	ConvNeXt-T [24]	✗	33.4	51.8	35.3	19.4	41.1	50.7	36.8	31.0	30.2	27.0
	ResNet-18 [14]	✗	18.1	30.9	18.3	8.2	24.8	33.3	20.6	16.7	17.3	14.6
Gamma correction [12]	ConvNeXt-T [24]	✗	33.7	52.0	35.9	18.6	41.7	51.3	36.8	31.3	31.3	27.2
RAOD [34]	ConvNeXt-T [24]	✓	34.4	52.9	35.9	19.5	42.9	52.2	37.1	31.9	35.0	29.2
RAW-Adapter [8]	ResNet-18 [14]	✓	19.9	33.2	20.1	9.8	27.3	34.4	22.3	18.1	20.8	16.9
Ours	ConvNeXt-T [24]	✗	34.8	53.3	36.7	20.6	42.8	52.5	37.7	32.1	36.1	28.4
	ResNet-18 [14]	✗	22.3	36.6	23.5	11.3	29.3	36.3	25.4	20.1	22.4	18.6

Table 5. Comparison with methods that adapt models pre-trained on sRGB domain to RAW images.

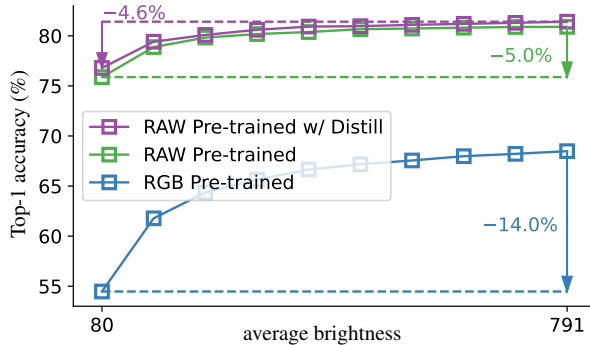


Figure 5. Top-1 accuracy on ImageNet-RAW when synthesizing RAW images under different average brightness. The maximum average brightness for an image is  $2^{16}$ .

**RAW pre-training with cross-domain distillation.** By replacing the sRGB input with synthetic RAW images, we can pre-train models using the classification targets provided by the original ImageNet-1K dataset and keep the hyper-parameters consistent with sRGB pre-training. However, due to the noise in RAW images, it is more difficult for the models to learn high-quality representations in the RAW domain than in the sRGB domain. For example, the ConvNeXt-T pre-trained on ImageNet-1K can achieve 82.1% Top-1 accuracy when testing on the sRGB domain. However, the model pre-trained on synthesized ImageNet-RAW only achieves 81.3% Top-1 accuracy when testing on the RAW domain. To alleviate this problem, we propose using the knowledge distillation [16, 32]. As cross-domain distillation, we take an off-the-shelf model pre-trained on the sRGB domain as the teacher to assist the pre-training on the RAW domain. The student shares the same architecture as the teacher for a fair comparison. Specifically, a logit distillation with the Kullback-Leibler divergence loss and a feature distillation with the L1 loss are combined. The supplementary material shows the details and ablation studies. **Enhanced robustness to adverse conditions.** RAW pre-training and cross-domain distillation enhance the robustness to different conditions. For one sRGB image, when converted to RAW at different epochs of pre-training, its brightness will be randomly adjusted, and random noise will be added. Meanwhile, the distillation provides consis-

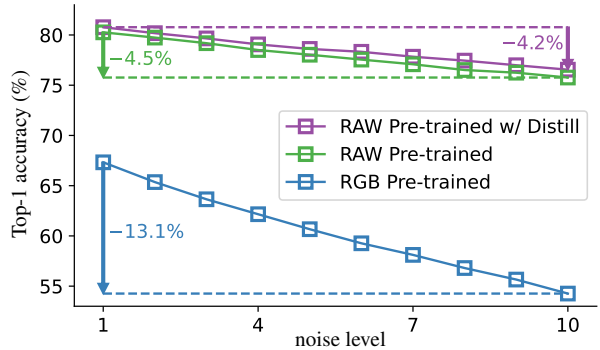


Figure 6. Top-1 accuracy on ImageNet-RAW when adding different noise levels to synthesized RAW images. Here, the noise level represents the standard deviation of the shot noises.

tent targets regardless of synthesized noise and brightness. Thus, the models are prompted to learn representations invariant to those conditions.

Fig. 5 and Fig. 6 verify the effects on robustness. By synthesizing the ImageNet-RAW validation set under different brightness and noise levels and evaluating the pre-trained models, we can observe that models pre-trained using distillation exhibit greater robustness to adverse conditions. For example, when reducing the brightness from 791 to 80, the performance degradation is 4.6% Top-1 accuracy when distillation, lower than 5.0% without distillation. Similarly, when increasing the noise level from 1 to 10, distillation exhibits a lower performance gap, *i.e.*, 4.2% vs 4.5%. In addition, we show that sRGB pre-training has a significantly higher performance degradation of 14.0% and 13.1% when adjusting the brightness and noise, respectively, showing that RAW pre-training effectively enhances the robustness.

## 5.2. Experiments Results.

Through RAW pre-training and distillation, ConvNeXt-T achieves 81.8% Top-1 accuracy on synthetic ImageNet-RAW. Although pre-training accuracy is still lower than sRGB pre-training (82.1%), the performance on real RAW object detection has significantly improved across various architectures, as shown in Tab. 3. For instance, RAW pre-training improves Cascade RCNN and ConvNeXt-T by 1.1% AP than sRGB pre-training. In particular, the mod-



Method	Backbone	Pre-Train	Fine-Tune	AP	AP <sub>50</sub>	AP <sub>75</sub>	AP <sub>s</sub>	AP <sub>m</sub>	AP <sub>l</sub>	AP <sub>normal</sub>	AP <sub>low</sub>	AP <sub>rain</sub>	AP <sub>fog</sub>
Cascade RCNN	Swin-T	sRGB	sRGB	28.1	44.6	29.0	11.1	20.1	33.9	30.5	26.4	32.3	23.2
Cascade RCNN	ConvNeXt-T	sRGB	sRGB	29.9	46.5	31.0	12.7	24.0	35.5	33.1	28.0	33.0	27.8
Cascade RCNN	Swin-T	sRGB	RAW	29.2	46.2	30.2	10.9	19.8	35.1	31.0	27.8	32.3	24.6
Cascade RCNN	ConvNeXt-T	sRGB	RAW	29.7	46.9	30.6	11.5	22.2	35.4	32.3	27.8	33.1	27.0
Cascade RCNN	Swin-T	RAW	RAW	29.8	47.0	30.9	11.4	21.7	35.4	31.4	28.1	32.9	27.3
Cascade RCNN	ConvNeXt-T	RAW	RAW	30.7	48.0	32.4	11.7	23.9	36.8	33.6	28.9	34.1	29.3

Table 6. Results of all-weather object detection using sliced RGB images.

Method	Params (M)	FPS	Epochs	AP	AP <sub>50</sub>	AP <sub>75</sub>	AP <sub>s</sub>	AP <sub>m</sub>	AP <sub>l</sub>	AP <sub>normal</sub>	AP <sub>low</sub>	AP <sub>rain</sub>	AP <sub>fog</sub>
YOLOX-Tiny [11]	5.1	222.6	300	16.4	32.1	14.9	6.8	23.2	29.4	18.0	15.2	15.1	12.3
YOLOv6-n [18]	4.3	170.7	400	18.0	30.0	18.0	7.6	24.4	32.8	19.3	16.0	16.5	14.0
YOLOv8-n [18]	3.0	188.1	500	18.9	32.0	18.8	8.9	26.5	33.2	21.4	16.3	16.8	15.4
YOLOv8-n [18] <sup>†</sup>	3.1	57.6	500	19.7	32.8	19.9	9.4	27.0	32.9	21.8	16.9	18.9	14.9
YOLO-MS-XS [6]	4.5	113.0	300	24.7	40.0	25.1	12.1	33.4	41.4	28.2	22.4	21.2	19.7

Table 7. Evaluation of real-time object detection using down-sampled images. The models are trained and evaluated with an input size of  $1280 \times 1280$ . <sup>†</sup> means using the trainable pre-processing module proposed by [34]. Meanwhile, we measure the frames per second (FPS) of all models using an NVIDIA 3090 GPU.

els achieve more significant improvements in adverse conditions, *i.e.*, 0.8% AP<sub>low</sub>, 4.8% AP<sub>rain</sub>, and 1.2% AP<sub>fog</sub> vs 0.9% AP<sub>normal</sub>. Compared to sRGB-based object detection, we improve by 0.8% AP. These results demonstrate the advantages of our RAW pre-training.

## 6. Experiments on Sliced AODRaw

The experiments in Section 4 and Section 5 use the down-sampling setting. Tab. 6 further lists the results of the slicing setting, where the hyper-parameters follow the down-sampling experiments, except that we fine-tune models for 12 epochs. The experiments with ConvNeXt show the same trends as those in Tab. 3. Adapting models pre-trained on the sRGB domain to RAW object detection degrades the AP by 0.2% compared to sRGB object detection, and RAW pre-training improves the performance by 0.8%. Differently, with the Swin transformer, RAW object detection outperforms sRGB object detection even when using sRGB pre-training. It may be because the sliced images contain more visual information, allowing the model to converge well compared to down-sampled images. Meanwhile, RAW pre-training further improves performance by 0.6% AP, especially in adverse conditions. Overall, these results further illustrate the effectiveness of RAW pre-training.

## 7. Experiments on Real-Time Object Detection

Besides the regular detectors in Tab. 3, we also evaluate real-time object detection of YOLO-Series. As shown in Tab. 7, YOLO-MS-XS [6] and YOLO-v8-n [18] achieve 24.7% and 18.9% AP with a high FPS and parameters less

than 5M. However, adverse conditions have lower performance, such as 16.3% AP<sub>low</sub>, 16.8% AP<sub>rain</sub>, and 15.4% AP<sub>low</sub> of YOLO-v8-n. Some methods have tried to boost the performance via a trainable ISP. Here, we take the recently proposed method [34] as an example for analysis. In Tab. 7, integrating [34] with YOLO-v8-n improves the performance to 16.9% AP<sub>low</sub> and 18.9% AP<sub>rain</sub>. However, the FPS is significantly reduced, destroying the real-time property of the detector. In summary, the proposed AODRaw provides a new foundation to push real-time RAW object detection development.

## 8. Conclusion

This paper introduces AODRaw, a challenging dataset for RAW-based object detection across diverse and adverse conditions. Compared to traditional sRGB datasets, AODRaw offers diverse RAW images that retain essential visual information for object detection in complex light and weather conditions. Based on AODRaw, we evaluate existing methods of RAW object detection. Meanwhile, we utilize a cross-domain knowledge distillation to directly pre-train models on the RAW domain, solving the domain gap between sRGB pre-training and RAW fine-tuning. In this way, we improve the performance, particularly in adverse conditions, without relying on extra pre-processing modules. Our dataset is a benchmark for evaluating detection methods and a foundation for developing detection methods that generalize well across varied conditions. Our insights highlight the potential of RAW pre-training to advance real-world object detection and encourage further research on exploiting RAW images for challenging environments.

## References

- [1] Mario Bijelic, Tobias Gruber, Fahim Mannan, Florian Kraus, Werner Ritter, Klaus Dietmayer, and Felix Heide. Seeing through fog without seeing fog: Deep multimodal sensor fusion in unseen adverse weather. In *CVPR*, 2020. 3
- [2] Tim Brooks, Ben Mildenhall, Tianfan Xue, Jiawen Chen, Dillon Sharlet, and Jonathan T Barron. Unprocessing images for learned raw denoising. In *CVPR*, 2019. 6
- [3] Zhaowei Cai and Nuno Vasconcelos. Cascade r-cnn: High quality object detection and instance segmentation. *IEEE TPAMI*, 2019. 2, 5, 6
- [4] Kai Chen, Jiaqi Wang, Jiangmiao Pang, Yuhang Cao, Yu Xiong, Xiaoxiao Li, Shuyang Sun, Wansen Feng, Ziwei Liu, Jiarui Xu, Zheng Zhang, Dazhi Cheng, Chenchen Zhu, Tianheng Cheng, Qijie Zhao, Buyu Li, Xin Lu, Rui Zhu, Yue Wu, Jifeng Dai, Jingdong Wang, Jianping Shi, Wanli Ouyang, Chen Change Loy, and Dahua Lin. MMDetection: Open mmlab detection toolbox and benchmark. *arXiv preprint arXiv:1906.07155*, 2019. 4, 5
- [5] Linwei Chen, Ying Fu, Kaixuan Wei, Dezhi Zheng, and Felix Heide. Instance segmentation in the dark. *International Journal of Computer Vision*, 131(8):2198–2218, 2023. 2
- [6] Yuming Chen, Xinbin Yuan, Ruiqi Wu, Jiabao Wang, Qibin Hou, and Ming-Ming Cheng. Yolo-ms: Rethinking multi-scale representation learning for real-time object detection. *arXiv preprint arXiv:2308.05480*, 2023. 8
- [7] Gong Cheng, Xiang Yuan, Xiwen Yao, Kebin Yan, Qinghua Zeng, Xingxing Xie, and Junwei Han. Towards large-scale small object detection: Survey and benchmarks. *IEEE TPAMI*, 45(11):13467–13488, 2023. 5
- [8] Ziteng Cui and Tatsuya Harada. Raw-adapter: Adapting pre-trained visual model to camera raw images. In *ECCV*, 2024. 1, 2, 3, 6, 7
- [9] Steven Diamond, Vincent Sitzmann, Frank Julca-Aguilar, Stephen Boyd, Gordon Wetzstein, and Felix Heide. Dirty pixels: Towards end-to-end image processing and perception. *ACM Trans. Graph.*, 40(3), 2021. 2
- [10] M. Everingham, L. Gool, Christopher K. I. Williams, J. Winn, and Andrew Zisserman. The pascal visual object classes (voc) challenge. *IJCV*, 88:303–338, 2009. 1, 3
- [11] Zheng Ge, Songtao Liu, Feng Wang, Zeming Li, and Jian Sun. YOLOX: Exceeding yolo series in 2021. *arXiv preprint arXiv:2107.08430*, 2021. 2, 8
- [12] Hongwei Guo, Haitao He, and Mingyi Chen. Gamma correction for digital fringe projection profilometry. *Appl. Opt.*, 43(14):2906–2914, 2004. 7
- [13] Yanhui Guo, Fangzhou Luo, and Xiaolin Wu. Learning degradation-independent representations for camera isp pipelines. In *CVPR*, 2024. 2
- [14] Kaiming He, Xiangyu Zhang, Shaoqing Ren, and Jian Sun. Deep residual learning for image recognition. In *CVPR*, 2016. 6, 7
- [15] Kaiming He, Xinlei Chen, Saining Xie, Yanghao Li, Piotr Dollár, and Ross Girshick. Masked autoencoders are scalable vision learners. In *CVPR*, 2022. 6
- [16] Geoffrey Hinton. Distilling the knowledge in a neural network. *arXiv preprint arXiv:1503.02531*, 2015. 7
- [17] Yang Hong, Kaixuan Wei, Linwei Chen, and Ying Fu. Crafting object detection in very low light. In *BMVC*, 2021. 1, 3, 4
- [18] Glenn Jocher, Ayush Chaurasia, and Jing Qiu. YOLO by Ultralytics, 2023. 8
- [19] Xiang Li, Wenhai Wang, Lijun Wu, Shuo Chen, Xiaolin Hu, Jun Li, Jinhui Tang, and Jian Yang. Generalized focal loss: Learning qualified and distributed bounding boxes for dense object detection. In *NeurIPS*, 2020. 5, 6
- [20] Zhihao Li, Ming Lu, Xu Zhang, Xin Feng, M. Salman Asif, and Zhan Ma. Efficient visual computing with camera raw snapshots. *IEEE TPAMI*, 46(7):4684–4701, 2024. 2, 4
- [21] Tsung-Yi Lin, Michael Maire, Serge Belongie, James Hays, Pietro Perona, Deva Ramanan, Piotr Dollár, and C Lawrence Zitnick. Microsoft coco: Common objects in context. In *ECCV*, 2014. 1, 2, 3, 5
- [22] Tsung-Yi Lin, Priya Goyal, Ross Girshick, Kaiming He, and Piotr Dollár. Focal loss for dense object detection. In *ICCV*, 2017. 2, 5, 6
- [23] Ze Liu, Yutong Lin, Yue Cao, Han Hu, Yixuan Wei, Zheng Zhang, Stephen Lin, and Baining Guo. Swin transformer: Hierarchical vision transformer using shifted windows. In *ICCV*, 2021. 6
- [24] Zhuang Liu, Hanzi Mao, Chao-Yuan Wu, Christoph Feichtenhofer, Trevor Darrell, and Saining Xie. A convnet for the 2020s. In *CVPR*, 2022. 2, 6, 7
- [25] Ali Mosleh, Avinash Sharma, Emmanuel Onzon, Fahim Mannan, Nicolas Robidoux, and Felix Heide. Hardware-in-the-loop end-to-end optimization of camera image processing pipelines. In *CVPR*, 2020. 1, 2, 3
- [26] Alex Omid-Zohoor, David Ta, and Boris Murmann. Pascalraw: raw image database for object detection. *Stanford Digital Repository*, 2014. 1, 3, 4
- [27] Haina Qin, Longfei Han, Juan Wang, Congxuan Zhang, Yanwei Li, Bing Li, and Weiming Hu. Attention-aware learning for hyperparameter prediction in image processing pipelines. In *ECCV*, 2022. 2
- [28] Shaoqing Ren, Kaiming He, Ross Girshick, and Jian Sun. Faster r-cnn: Towards real-time object detection with region proposal networks. *IEEE TPAMI*, 2017. 2, 5, 6
- [29] Olga Russakovsky, Jia Deng, Hao Su, Jonathan Krause, Sanjeev Satheesh, Sean Ma, Zhiheng Huang, Andrej Karpathy, Aditya Khosla, Michael Bernstein, et al. Imagenet large scale visual recognition challenge. *IJCV*, 2015. 6
- [30] Peize Sun, Rufeng Zhang, Yi Jiang, Tao Kong, Chenfeng Xu, Wei Zhan, Masayoshi Tomizuka, Lei Li, Zehuan Yuan, Changhu Wang, and Ping Luo. Sparse r-cnn: End-to-end object detection with learnable proposals. In *CVPR*, 2021. 2, 5, 6
- [31] Yujin Wang, Tianyi Xu, Fan Zhang, Tianfan Xue, and Jinwei Gu. Adaptiveisp: Learning an adaptive image signal processor for object detection. In *NeurIPS*, 2024. 2
- [32] Yixuan Wei, Han Hu, Zhenda Xie, Zheng Zhang, Yue Cao, Jianmin Bao, Dong Chen, and Baining Guo. Contrastive learning rivals masked image modeling in fine-tuning via feature distillation. *arXiv preprint arXiv:2205.14141*, 2022. 7

- [33] Chyuan-Tyng Wu, Leo F. Isikdogan, Sushma Rao, Bhavin Nayak, Timo Gerasimow, Aleksandar Susic, Liron Ainkedem, and Gilad Michael. Visionisp: Repurposing the image signal processor for computer vision applications. In *ICIP*, 2019. [2](#)
- [34] Ruikang Xu, Chang Chen, Jingyang Peng, Cheng Li, Yibin Huang, Fenglong Song, Youliang Yan, and Zhiwei Xiong. Toward raw object detection: A new benchmark and a new model. In *CVPR*, 2023. [1](#), [2](#), [3](#), [4](#), [6](#), [7](#), [8](#)
- [35] Masakazu Yoshimura, Junji Otsuka, Atsushi Irie, and Takeshi Ohashi. Dynamicisp: Dynamically controlled image signal processor for image recognition. In *ICCV*, 2023. [2](#)
- [36] Ke Yu, Zexian Li, Yue Peng, Chen Change Loy, and Jinwei Gu. Reconfigisp: Reconfigurable camera image processing pipeline. In *ICCV*, 2021. [2](#), [4](#)
- [37] Bo Zhang, Yuchen Guo, Runzhao Yang, Zhihong Zhang, Jiayi Xie, Jinli Suo, and Qionghai Dai. Darkvision: a benchmark for low-light image/video perception. *arXiv preprint arXiv:2301.06269*, 2023. [3](#)
- [38] Xizhou Zhu, Weijie Su, Lewei Lu, Bin Li, Xiaogang Wang, and Jifeng Dai. Deformable detr: Deformable transformers for end-to-end object detection. In *ICLR*, 2021. [2](#), [4](#), [5](#), [6](#)



# Towards RAW Object Detection in Diverse Conditions

## Supplementary Material

### 9. Statistics of AODRaw

**More examples from AODRaw.** We collect images under 9 conditions, as shown in Tab. 2 of the main paper. Tab. 9 shows a **specific example for each condition** for a better understanding. Furthermore, Fig. 7 shows **more examples of our AODRaw dataset** and the annotated bounding boxes, showing the diversity of the AODRaw.

**Visualization of RAW images.** To better show the domain gap between RAW and sRGB images, we show some RAW images and the corresponding sRGB images in Fig. 8. Here, the RAW images are visualized by demosaicing and normalizing them to the range of [0, 255], without any other preprocessing operations.

**Annotated categories.** Tab. 10 lists the categories in AODRaw and the corresponding number of instances. We sort the categories according to the number of instances.

**Categories per image.** Fig. 9 shows the distribution of the number of categories in the images. For each condition, the maximum number of categories exceeds 10. More than half of the conditions have a maximum number that exceeds 15. Especially, the maximum number for the indoor low-light condition is 19.

**Instances per image.** Fig. 10 shows the distribution of the number of instances in images. In all conditions, there are complex images containing hundreds of instances. The distribution of a single condition is close to the overall distribution, especially when the number of instances is less than 100. For cases exceeding 100, since there are fewer images in this range, there is some deviation between several conditions and the whole, *e.g.*, the condition of low-light and fog in outdoor scenes, as shown in Fig. 10h.

**Bounding box size.** Fig. 11 shows the distribution of the bounding box size for each condition, where small objects account for the majority in all conditions. Meanwhile, compared to the overall distribution of all conditions, the images in indoor scenes contain fewer small objects and more large objects, as shown in Fig. 11a and Fig. 11b. In contrast, the outdoor scenes have a similar distribution to the overall distribution with a large number of small objects.

### 10. Experiments Settings

Most hyperparameters follow the COCO dataset in the mmdetection. For data augmentations, the images are resized between 800 and 1024 along the shorter side, while the longer side is no larger than 2048. And the RandomFlip is used to augment images. For detectors using ConvNeXt, we set the layer-wise learning rate decay as 0.75 and the stochastic depth (DropPath) ratio as 0.4. For detectors us-

Distillation	AP	AP <sub>50</sub>	AP <sub>75</sub>
$\times$	34.1	52.4	35.9
Logit	34.3	52.4	36.6
Logit + Feature	34.8	53.3	36.7

Table 8. Ablation for the knowledge distillation when using Cascade RCNN and ConvNeXt-T.

ing Swin-T, the stochastic depth ratio is 0.2. For RAW pre-training, we follow the official codes released by ConvNeXt and Swin.

### 11. Distillation Implementation

**Method.** Besides the supervised classification loss function, we use logit-based and feature-based distillation for cross-domain distillation. For logit-based distillation, we denote  $z_s$  and  $z_t$  as the output of student and teacher, respectively.  $z_s$  and  $z_t$  have been normalized by the SoftMax function. Then, the logit-based loss is calculated as follows:

$$L_l = \text{KLDivLoss}(y_s, y_t) = y_t \log \frac{y_t}{y_s}. \quad (1)$$

For feature-based distillation, we denote  $z_s$  and  $z_t$  as the global feature output by the student and teacher, respectively. For ConvNeXt, the features are acquired through 1) applying global average pooling to the output of the last block and 2) processing the feature using the last Layer-Norm layer. The loss is calculated as follows:

$$L_f = \frac{1}{C} \sum_{i=0}^{C-1} |z_s^i - z_t^i|, \quad (2)$$

where C means the number of dimensions.

**Ablation studies.** We ablate the two types of distillation in Tab. 8. Logit-based distillation improves the AP by 0.2%, and feature-based distillation further extends the improvement by 0.5%.

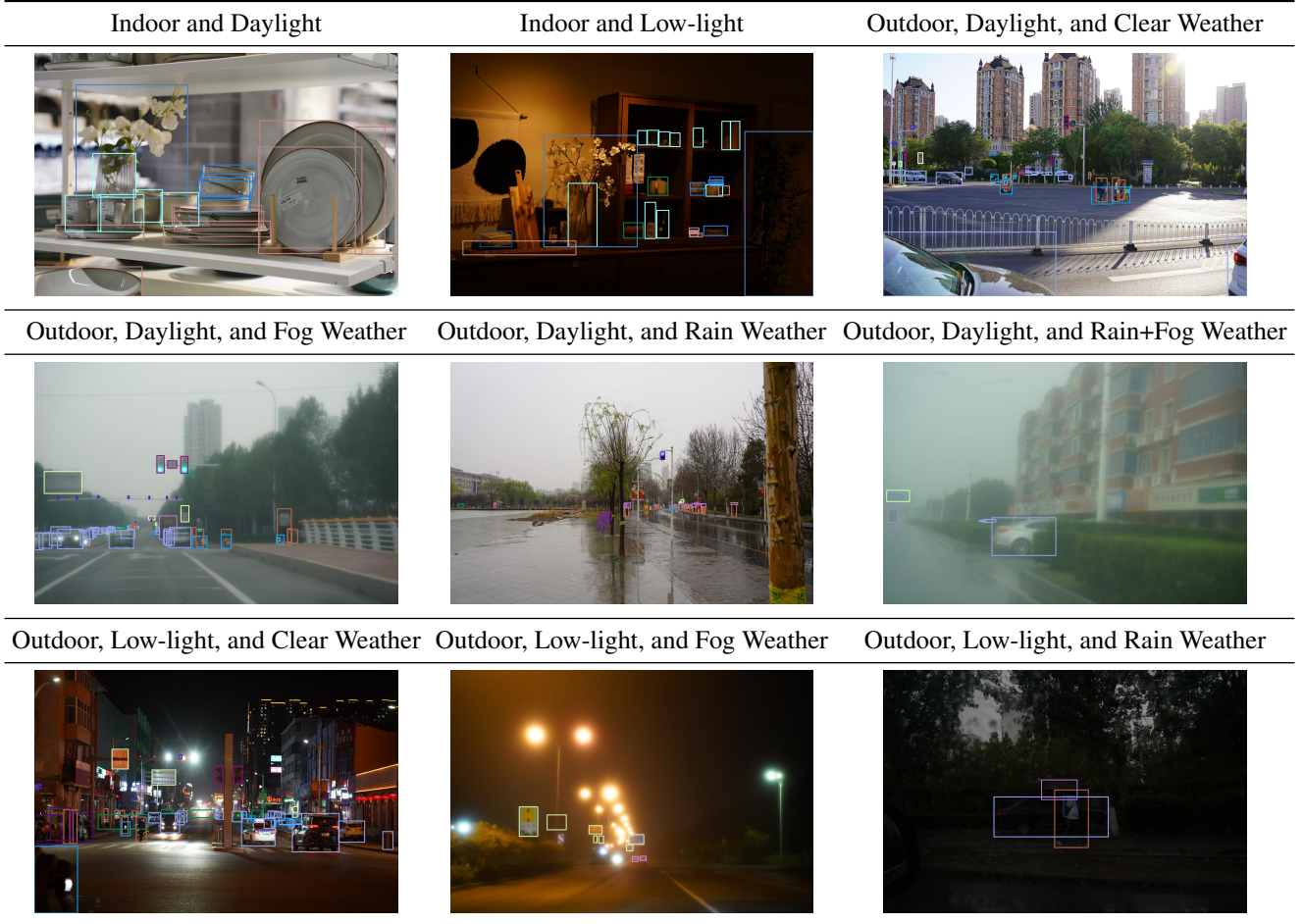


Table 9. The example of each condition in AODRaw.

Name	Instance	Name	Instance	Name	Instance	Name	Instance
car	42798	person	16864	traffic sign	13458	surveillance camera	9344
traffic light	8884	motorcycle	7389	truck	4271	chair	3548
bottle/cup	3168	bicycle	2134	garbage can	1993	traffic cone	1929
table	1480	tricycle	1268	helmet	1211	umbrella	1142
pillow	1055	lamp	1046	handbag/satchel	1001	bus	973
potted plant	910	hat	893	backpack	818	phone	685
plate	663	vase	639	monitor	586	bus stop sign	528
desk lamp	431	tent	406	sofa	373	clock	333
bowl	322	pen	228	crane	196	wine glass	191
bench	191	keyboard	175	mirror	170	bed	158
mouse	155	pot	151	earphone	151	fire hydrant	145
toilet paper	138	spoon	105	laptop	104	sink	96
watch	93	fire extinguisher	90	suitcase	85	train	72
dog	64	computer box	58	refrigerator	43	cans	42
vending machine	34	airplane	32	boat	29	cat	23
toilet	20	scissors	19				

Table 10. The annotated categories and the number of instances per category.



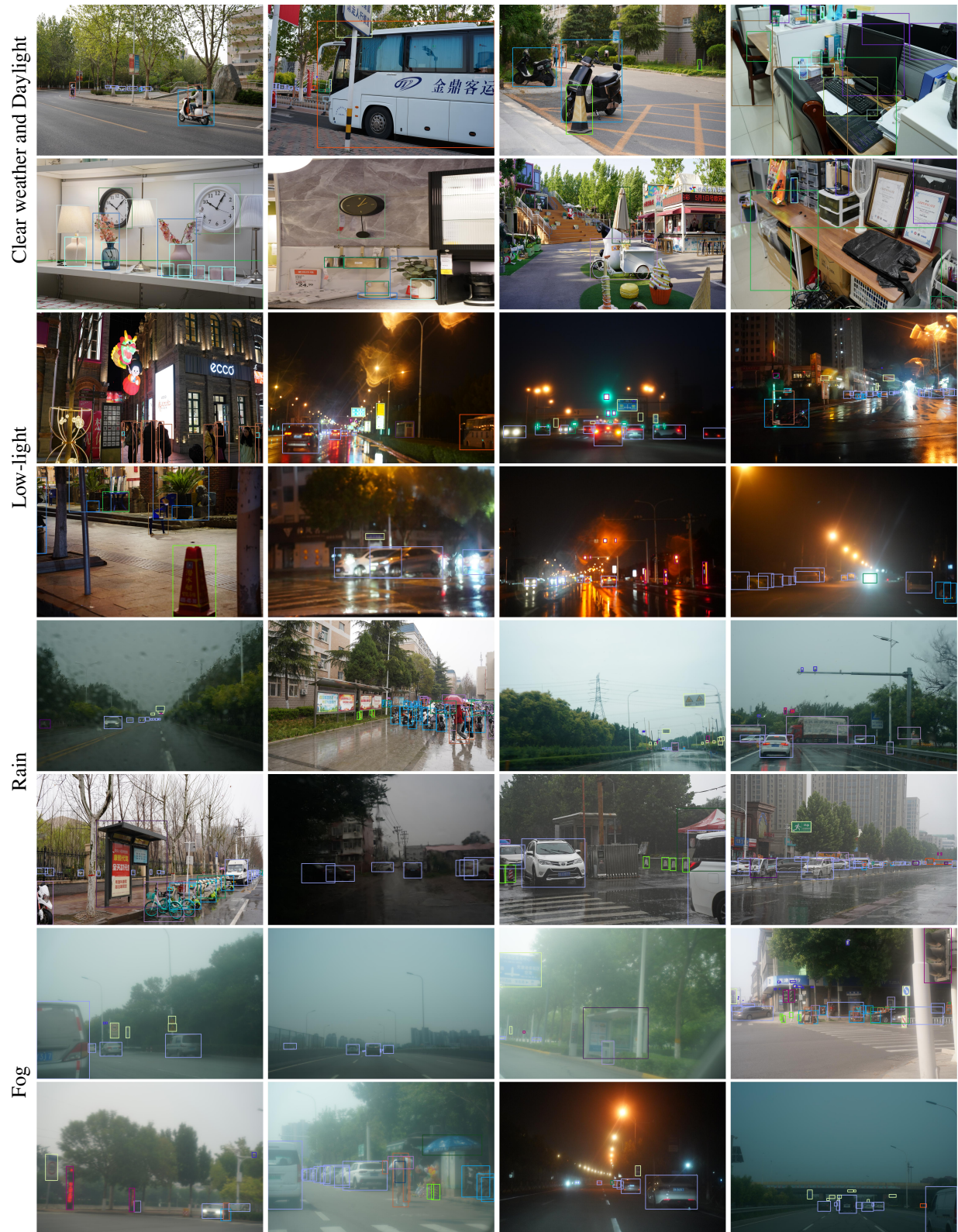


Figure 7. Example of the images in the AODRaw.





RAW

sRGB

RAW

sRGB

Figure 8. Example of the RAW images in the AODRaw.

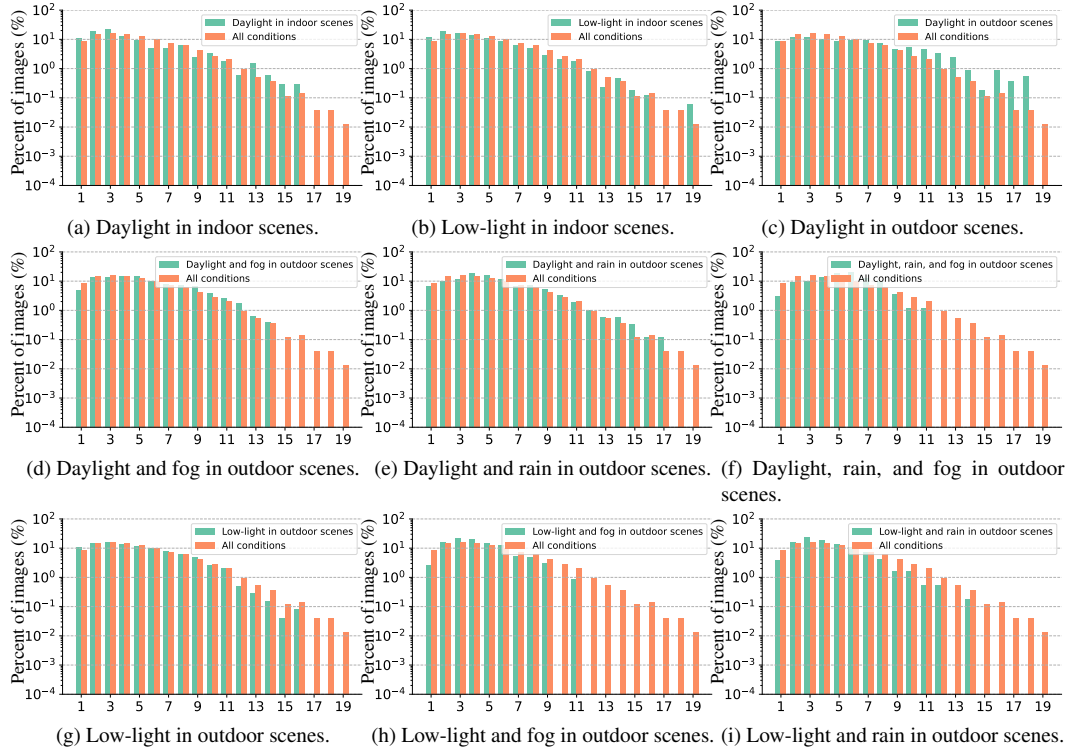


Figure 9. Distribution of the number of categories in images of each condition. The horizontal axis represents the number of categories.

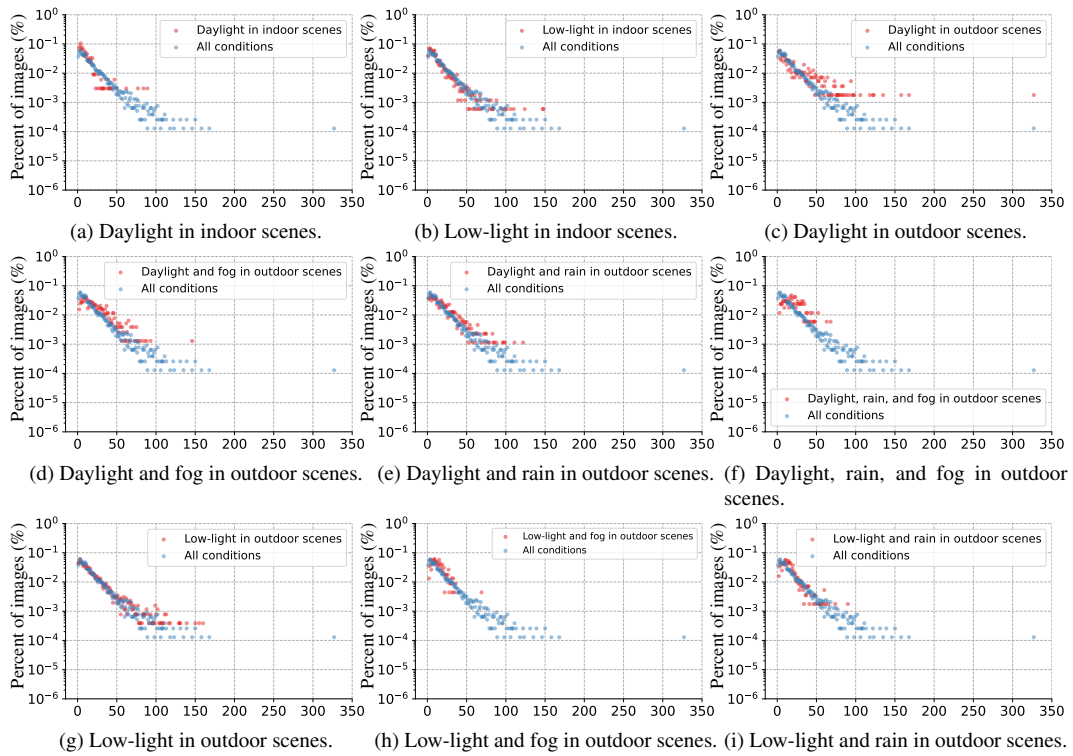


Figure 10. Distribution of the number of instances in images of each condition. The horizontal axis represents the number of instances.

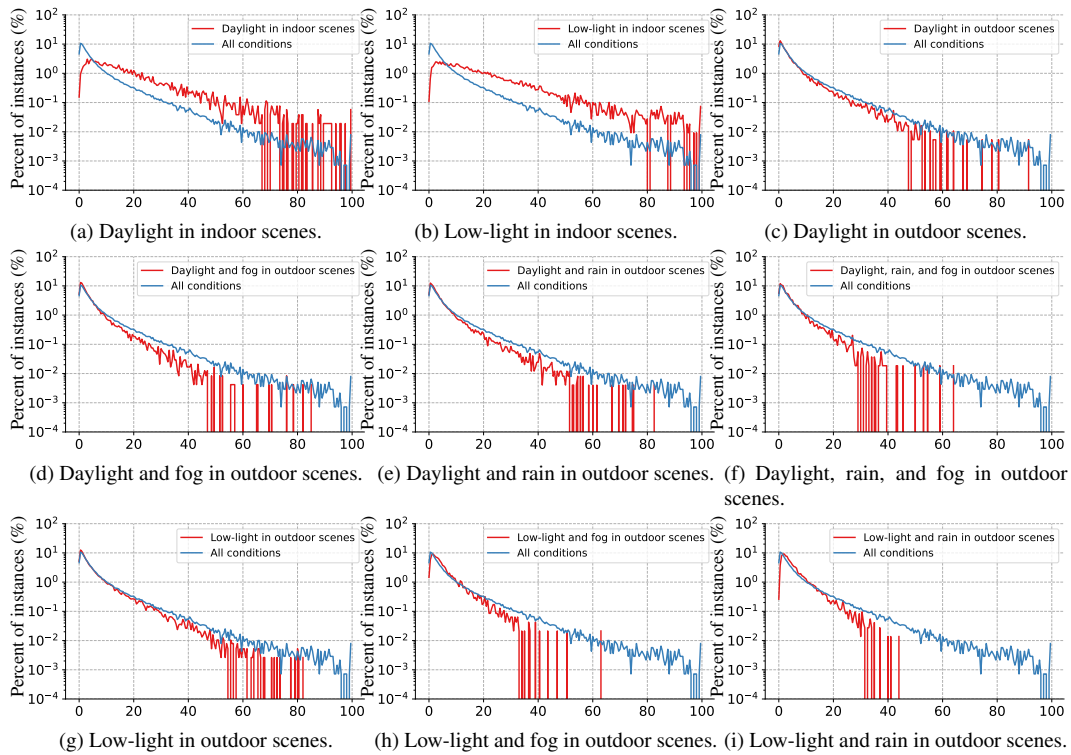


Figure 11. Relative bounding box size  $\sqrt{\frac{\text{box area}}{\text{image area}}}$  of each condition. The horizontal axis represents the relative bounding box size.